

Supplementary Information

Spin phase protection in interference of electron spin waves of lightly hydrogenated graphene

T. Kato¹, J. Kamijo¹, T. Nakamura², C. Ohata¹, S. Katsumoto², and J. Haruyama¹

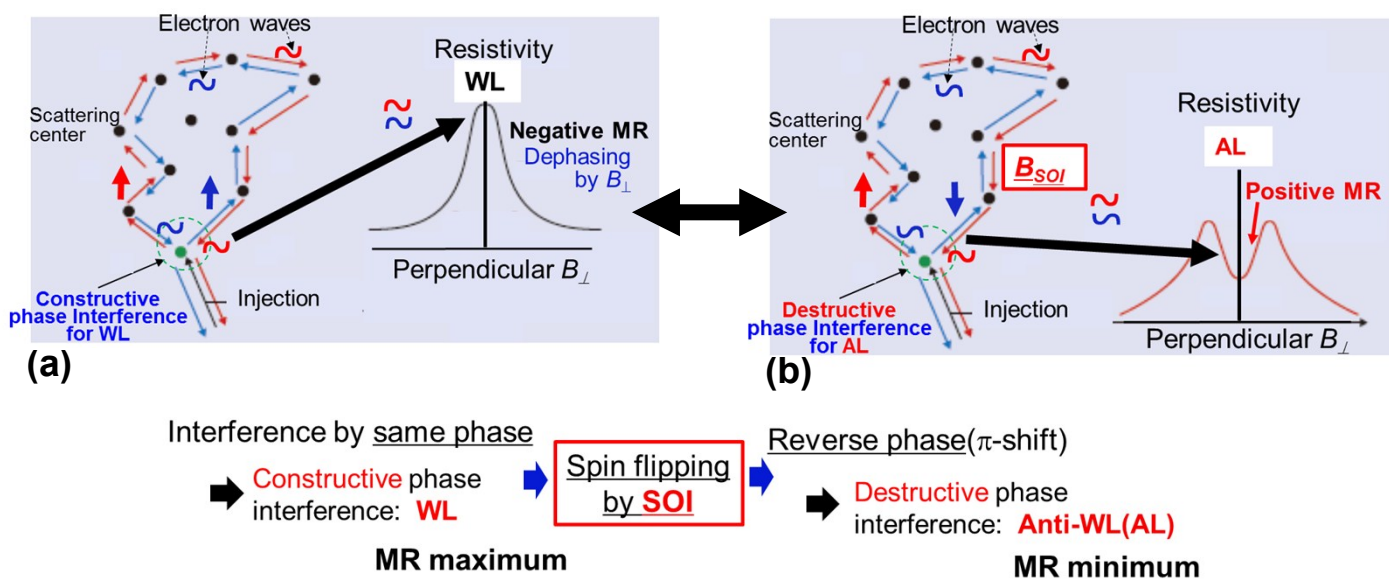
Faculty of Science and Engineering, Aoyama Gakuin University, 5-10-1 Fuchinobe, Sagami-hara, Kanagawa 252-5258, JAPAN

²Institute for Solid State Physics, The Tokyo University, 5-1-5 Kashiwanoha, Kashiwa, Chiba 277-8581, Japan

*Corresponding author: J-haru@ee.aoyama.ac.jp (J.H.)

(1) Phase interference phenomena of electron waves

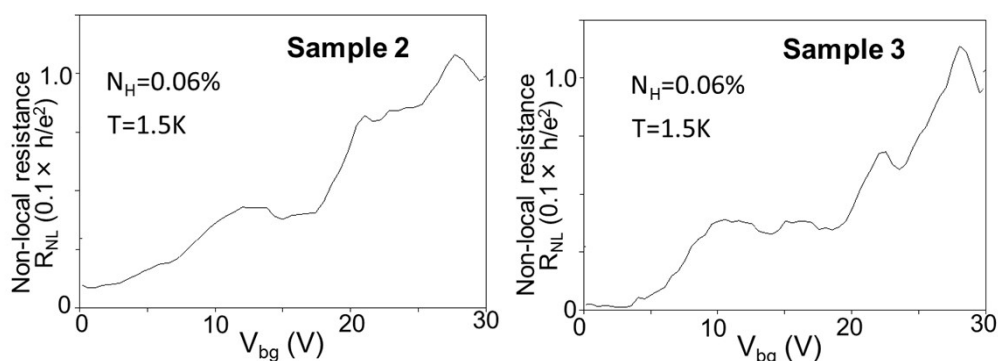
When the sample size is smaller than or comparable to the phase coherence length L_ϕ or thermal diffusion length L_{th} (i.e., within a diffusive electron transport regime), the electron spin phases are preserved throughout the entire sample even with some scattering centers^{17, 26-29}. This causes various phase interference of the electron spin waves (S-Fig. 1a), e.g., weak localization (WL), which is a constructive phase interference between two partial electron waves encircling a 2D plane in opposite directions along time-reversal symmetry paths and shows a magnetoresistance (MR) peak with negative MR due to dephasing by applied perpendicular B , and anti-localization (AL), which is a destructive interference and exhibits a MR minimum with positive MR (S-Fig. 1b); Altshuler-Aronov-Spivak (AAS) oscillation with a constant normalized period of $\Delta B \propto (1/2)(h/e)$ where h is the Planck's constant and e is the elemental charge of electron, which originates from modulation of the vector potential existing in an inner space of cylindrical structures (with phase interference path between partial waves encircling in opposite direction) by penetrating magnetic flux, universal conductance fluctuation (UCF). Importantly, SOI is known to scatter the electron spin, leading to a flip of the spin moment, and then a transfer of WL to AL through phase shift in π in thin metals, semiconductor 2DEG, and CNTs. Absence of SOI and, thus, strong spin coherence without this spin flip is a benefit of graphene for spintronics.



S-Fig.1: Schematic views of WL (a), and AL (b) caused by spin flip due to SOI in conventional 2D materials.

(2) Measurement examples of reproducibility in other two samples

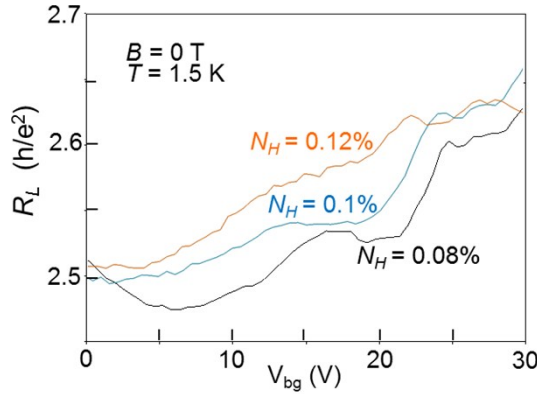
We have observed qualitatively similar results at least in five samples. For example, R vs. V_{bg} features in two samples with the same N_H of 0.06% are shown in S-Fig.2 as below. Although shapes of R peaks are different, they certainly exhibit some R peaks around similar V_{bg} 's, which show strong association with WL in temperature and magnetic field measurements.



S-Fig.2: R vs. V_{bg} features in two samples with the same N_H of 0.06%

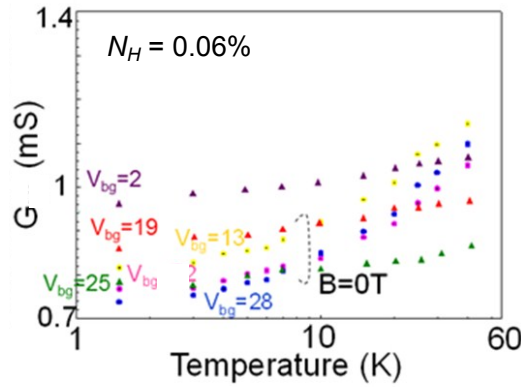
(3) Results of local two-probe resistance measurements in high N_H regime ($> 0.06\%$)

S-Figure 3 shows two-probe local resistance (R_L) measurement in high N_H regime ($> 0.06\%$), using electrodes 3 and 4. Resistance peaks like Fig. 2a in text are not evidently observed. R_L peak (conductance minimum) at $N_H = 0.06\%$ shown in inset of Fig. 2a in text becomes broad and ambiguous at $N_H = 0.08\%$, while other peak like feature appears at high V_{bg} . At $N_H = 0.12\%$, both features disappear. These suggest validity to detection of WL in graphene with the present small N_H regime ($< 0.06\%$) in text.



S-Fig. 3: two-probe local resistance (R_L) measurement as a function of V_{bg} in high N_H regime ($> 0.06\%$).

(4) Temperature dependence of G at three V_{bg} 's, corresponding to R minimum in Fig. 2a.



S-Fig. 4: Temperature dependence of G at three V_{bg} 's (= 2V, 19V, and 25V; Δ symbols), which approximately correspond to R minimum in Fig. 2a.

The temperature dependence of G at three V_{bg} 's (= 2V, 19V, and 25V; Δ symbols), which approximately correspond to R minimum in Fig. 2a, is shown in S-Fig.4. They show weak temperature dependence meaning small strength of WL, which are different from those observed at the three R peaks suggesting WL (Fig. 3). This result evidently suggests that the observed WL behavior appears only at the optimum V_{bg} 's, which can provide the most suitable electron spin density (via SHE) to yield phase interference loop path for WL (like the case of orbital quantization).

In conventional case, WL occurs when phase coherence is preserved through all sample region. However, strength of WL depends on impurity and electron densities. In particular, in present case, the accumulated electron spins form phase interference loop path for WL (Fig. 1d). Therefore, the optimum V_{bg} 's, which correspond to the three R peaks in Fig. 2a, should exist for it.

(5) High critical temperature with small L_{so}

The critical temperature (T_c) between the high and low temperature regions is significantly different from other 2D materials. The best fit by the WL formula gave $p = 4$ for $W = 4 \mu\text{m}$ and $L = 24 \mu\text{m}$ for the present H -graphene.

The fitted p value suggests dephasing of spin phase interference by electron-electron interactions, as in multi-walled CNTs. In contrast, T_c of ~ 6 K, for low-temperature saturation at $B = 0$ T, is considerably higher than that observed in CNTs (e.g., $T_c = 0.3$ K for $B = 0$ T). In conventional 2D materials, the phase relaxation length ($L_\phi(T) = \sqrt{D\tau_\phi}$) is given by $\tau_\phi^{-1}(T) = \tau_{in}^{-1}(T) + 2\tau_s^{-1}$ (where D is the diffusion constant, and τ_ϕ , τ_{in} , and τ_s are the relaxation times for phase coherence, and inelastic and magnetic spin scattering, respectively). At $T > T_c$ for $\tau_{in}(T)^{-1} \gg \tau_s^{-1}$, dephasing is dominated by inelastic scattering factors reflected in the p value, whereas at $T < T_c$ for $\tau_{in}(T)^{-1} \ll \tau_s^{-1}$, magnetic spin scattering (which is largely independent of temperature) dominates the dephasing. Thus, a T_c of as high as ~ 6 K suggests the presence of a larger τ_s^{-1} rate. On the other hand, our graphene samples, which were mechanically exfoliated from graphite, contain no magnetic impurities, which we carefully checked by superconducting quantum interference devices (quantum design). Thus, the high T_c can be possibly attributed to the SOI scattering rate τ_{so}^{-1} , rather than τ_s^{-1} . This implies that the possible SOI suppresses dephasing arising from electron-electron interaction at high temperatures. Indeed, T_c increases with increasing N_H (i.e., increasing SOI), as shown in the inset of Fig. 3.

(6) Data fitting method to temperature dependence by taking τ_{SOI} into consideration for T_c

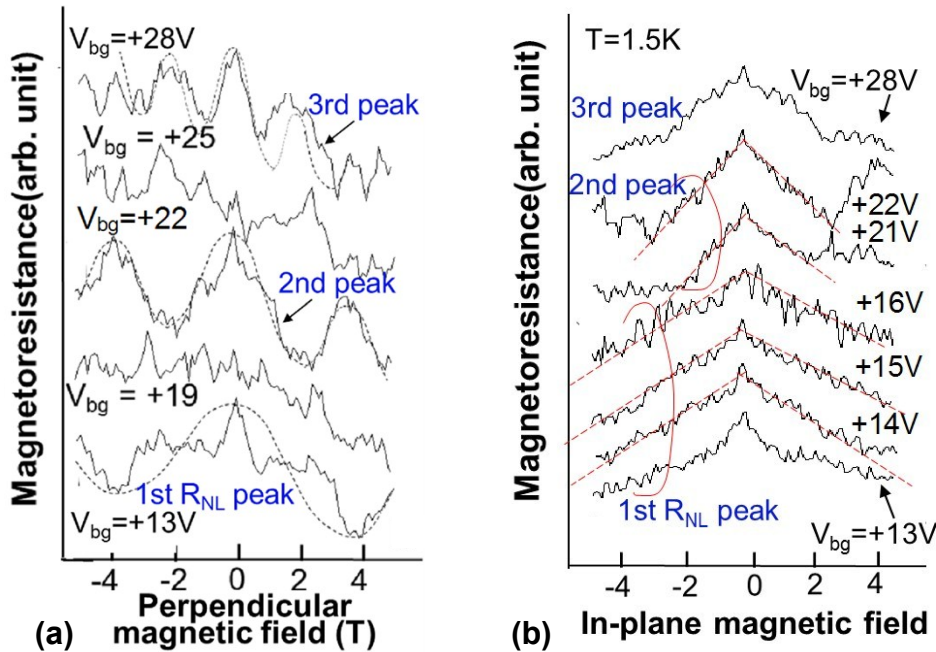
In conventional 2D materials, presence of SOI leads to negative conductance for temperature increase (i.e., AL due to spin flip caused by SOI: SO (2)). Thus, the term given by $(-3/2)\log[1+(T/T_c)^p]$ is added to conventional WL formula. In contrast, in the case of graphene, SOI does not lead to spin flip. Thus, the term given by $\log\{1+[T/(T_c+T_c')^p]\}$ was added in

eq.(1) of text. In ref.9, similar correction was taken into consideration for influence of SOI to WL correction when perpendicular magnetic field was applied.

(6) Calculation method for the contribution of the SOI to the negative MR in WL under perpendicular magnetic fields

Negative MRs in Figs. 4a and 4c were fit as follows. Employing the L_{SOI} value $L_{SOI} \sim 2 \mu\text{m}$, $\beta = 2$, $r = 20 \text{ nm}$, $N = 1$, and $L_\phi/L_\phi' = 4/3$, we can obtain the best fitting to the negative MR for $N_H = 0.06\%$ (dotted curve in Fig. 4c). In contrast, using $L_{SOI} \sim 10 \mu\text{m}$ cannot give good agreement (blue dotted curve in Fig. 4c) in any parameters.

(7) All MR curves observed under perpendicular and in-plane magnetic fields at $N_H = 0.06\%$.



S-Fig. 5: (a) MRs at all measured V_{bg} 's around $B = 0$ and in large B region, when perpendicular B is applied. They include Fig. 4a,c and S-Fig.6. Negative MRs and periodic oscillations are observed only around the three R peaks for Fig. 2a (i.e., $V_{bg} = +13, +22, \text{ and } +28 \text{ V}$).

(b) Negative MR behaviours including Fig. 4d in text, when in-plane B is applied. They show linear slope only around the three R peaks in Fig. 2a. MRs at $V_{bg} = +13\text{--}16 \text{ V}$ correspond to the first broad R peak in Fig. 2a. MRs at $V_{bg} = +21$ and $+22 \text{ V}$ correspond to the second, and MR at $V_{bg} = +23 \text{ V}$ to the third R peak, respectively.

(8) Suppression of dephasing even at high B ; Possible AAS oscillation

The AAS oscillations arise from the modulation of the vector potential confined within an inner cylindrical region (that originates from phase interference paths between partial waves encircling along a cylinder in opposite direction, like those for WL) by penetrating magnetic flux. Such phase interference loop paths (i.e., that for WL in the present case) should be eliminated at high B in 2D structures, graphene, and hence AAS oscillations should not be observed.

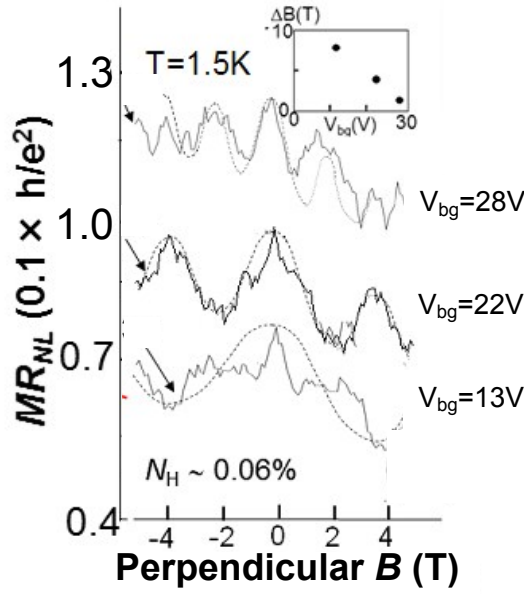
In the analysis for Fig. 4, we focused on the negative MRs only around $B = 0$. On the other hand, when a higher perpendicular B is considered for $\pm 5\text{T}$, periodic MR oscillations appear, as shown below in S-Fig. 6. Because these oscillations are observed only to the three R_{NL} peaks as well as those for temperature dependence of WL (Fig. 3), phase interference is strongly associated. One possibility may be Altshuler-Aronov-Spivak (AAS) oscillations with a constant normalized period $\Delta B \propto (1/2)(h/e)$, where h is the Planck's constant and e is the elemental charge of the electron (SI (1)). S-Fig. 6 can be fitted by the theory (dotted curves and SI (10)), when presence of very small AAS loop (e.g., $10 \sim 100\text{nm}$) is assumed.

If the oscillation would be due to AAS effect, one possible interpretation for the observed large oscillation periods, which correspond to $10 - 100 \text{ nm}$ of the area diameter for the interference loop path, may be series connection of multiple AAS loops. Previously, oscillation period of $1/n$ was reported due to n -th encircling electron path on AAS loop in CNT. In contrast, series connection of n -AAS loops may yield n -times larger oscillation period based in it. In the present case, at least 40 AAS loops may be required for this between probes 1 and 2. Anyway, much detailed investigation is indispensable.

Moreover, we find that the oscillation period ΔB among the three R_{NL} peaks decreases by a factor of two after each V_{bg} increase ($\Delta B = 8, 4, \text{ and } 2 \text{ T}$ for $V_{bg} = 13, 22, \text{ and } 28 \text{ V}$, respectively; see inset of S-Fig.6). This suggests the presence of the AAS effect, arising from n -times-encircling paths around the AAS loop ($n = 1\text{--}3$; WL loop), which is characterized by $\Delta B \propto (1/2)^n (h/e) (\pi r^2)^{-1}$, as confirmed by fitting the data with the AAS theory. Because the AAS loop at $V_{bg} = 13 \text{ V}$ (corresponding to the Dirac point) is the most stable, the electron spins tend to circulate two- and three-times along the same AAS loop at the other two specified V_{bg} 's (i.e., 22 and 28 V) when a perpendicular B is applied. This can explain the three R

peaks that only appear at specified V_{bg} 's satisfying conditions appropriate for forming the WL path, and hence the AAS path with n -times encircling electron waves, as in the present case.

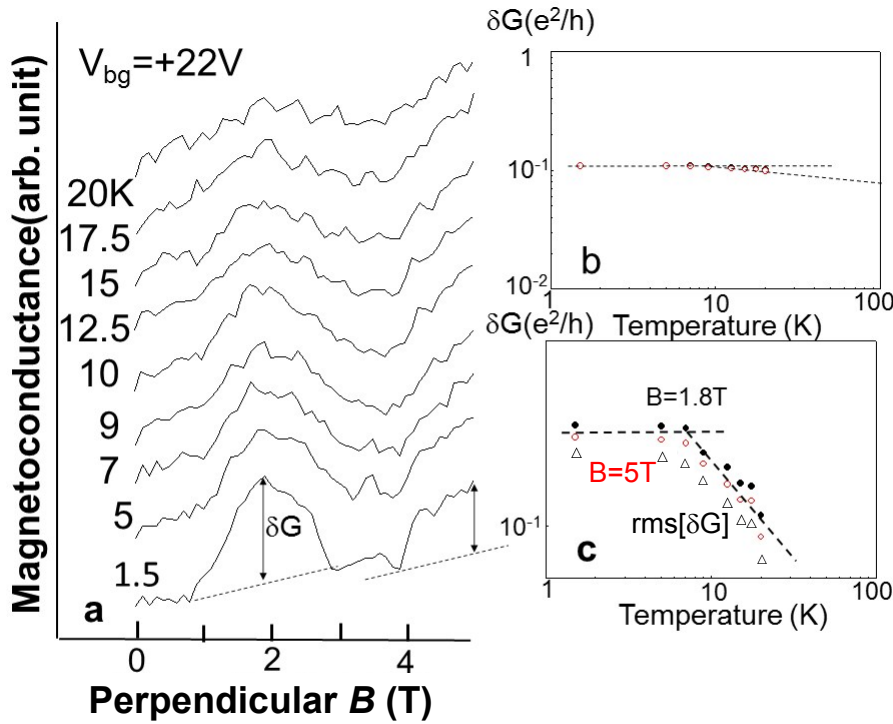
Although further investigation is indispensable, it implies that the SOI-based suppression of dephasing remains even at high B , because the AAS loop can exist only in tube-like structures in conventional cases and disappears as a result of dephasing caused by high B in conventional 2D materials.



S-Fig. 6 Perpendicular- B dependence of the three R peaks of Fig. 2(a) in the high B region. The dashed curves represent the best fits by the AAS theory performed with $L_{so} = 2 \mu\text{m}$.

Inset: Oscillation period ΔB estimated at three different V_{bg} 's shown in the main panel. Their halving with increasing V_{bg} suggests the presence of n -times ($n = 1-3$) encircling possible AAS loop.

(9) Possible universal conductance fluctuation (UCF)



S-Fig. 7: Magnetic field and temperature dependence of magnetoconductance (MC).

(a) Values calculated from MR at $V_{bg} = +22 \text{ V}$ in S-Fig.6. Two MC peaks exist around $B = 1.8$ and 5 T . Peak heights δG gradually decrease as temperature increases. (b) and (c) Double-logarithmic temperature dependence of δG at $B = 1.8 \text{ T}$ (black symbols) and 5 T (red symbols) estimated from S-Fig. 7a and the root-mean-square [δG] (triangle symbol) calculated from them. (c) is expansion of (b) along Y axis. Dotted lines are guides to the eyes. Values appear mostly constant in (b), whereas detailed observation reveals a slight decrease above 7 K following power law behavior ($\sim T^{-1/4}$).

Magneto conductance (MC) transformed from MR at $V_{bg} = 22 \text{ V}$ in S-Fig. 6 is shown as a function of the temperature and $B (> 0)$ in S-Fig. 7a. At low temperature, the conductance exhibits reproducible, periodic fluctuations, which are superimposed on the positive background caused by the WL and Landau level effects. These fluctuations are well known as the UCF. The root-mean-square (rms) amplitude of the fluctuation δG reaches the universal value $\sim e^2/h$, when the sample size \ll both L_ϕ and L_T . When either L_ϕ or L_T becomes smaller than L , the shorter of these governs the amplitude of the fluctuations, corresponding to the present case. S-Figs. 7b and 7c show a doubly logarithmic temperature dependence of δG at two B values estimated from S-Fig. 7a and $\text{rms}[\delta G]$. They appear mostly constant in S-Fig. 7b; however, an expansion along the Y axis (S-Fig. 7c) reveals a slight decrease above 7 K following power law behavior ($\sim T^{-1/4}$) owing to dephasing. This power value is smaller than those in the conventional UCF, which is proportional to $L_\phi \propto T^{-1/2}$; hence, it implies suppression of the dephasing. The present SOI will contribute significantly to this suppression, as well as to the WL and AAS oscillations.